




## Article

# Synthesis, Optical, Magnetic and Thermodynamic Properties of Rocksalt $\text{Li}_{1.3}\text{Nb}_{0.3}\text{Mn}_{0.4}\text{O}_2$ Cathode Material for Li-Ion Batteries

Mohamed Kamel <sup>1</sup>, Abanoub R. N. Hanna <sup>2,3</sup>, Cornelius Krellner <sup>4</sup>, Rüdiger Klingeler <sup>5,6</sup>, Mohamed Abdellah <sup>7,8</sup>, Mahmoud Abdel-Hafiez <sup>1,9,\*</sup>, Arafa Hassen <sup>1,\*</sup>, Ahmed S. G. Khalil <sup>1,10</sup>, Tarob Abdel-Baset <sup>1,11</sup> and Abdelwahab Hassan <sup>1</sup>

- <sup>1</sup> Physics Department, Faculty of Science, Fayoum University, El Fayoum 63514, Egypt; mmr06@fayoum.edu.eg (M.K.); asg05@fayoum.edu.eg (A.S.G.K.); taa03@fayoum.edu.eg (T.A.-B.); aha08@fayoum.edu.eg (A.H.)
- <sup>2</sup> Institut für Festkörperforschung, Technische Universität Berlin, Hardenbergstr. 36, 10623 Berlin, Germany; abanoub.hanna@helmholtz-Berlin.de
- <sup>3</sup> Helmholtz-Zentrum Berlin für Materialien und Energie, Hahn-Meitner Platz 1, 14109 Berlin, Germany
- <sup>4</sup> Physikalisches Institut, Goethe-Universität Frankfurt, 60438 Frankfurt am Main, Germany; krellner@physik.uni-frankfurt.de
- <sup>5</sup> Kirchhoff Institute of Physics, Heidelberg University, 69120 Heidelberg, Germany
- <sup>6</sup> Centre for Advanced Materials (CAM), Heidelberg University, 69120 Heidelberg, Germany; ruediger.klingeler@kip.uni-heidelberg.de
- <sup>7</sup> Ångström Laboratory, Department of Chemistry, Uppsala University, Box 523, 75120 Uppsala, Sweden; Mohamed.Qenawy@kemi.uu.se
- <sup>8</sup> Department of Chemistry, Qena Faculty of Science, South Valley University, Qena 83523, Egypt
- <sup>9</sup> Department of Physics and Astronomy, Uppsala University, 75120 Uppsala, Sweden
- <sup>10</sup> Materials Science and Engineering Department, School of Innovative Design Engineering, Egypt-Japan University of Science and Technology (E-JUST), P.O. Box 179, New Borg El-Arab City 21934, Egypt
- <sup>11</sup> Department of Physics, Faculty of Science, Taibah University, Yanbu 46423, Saudi Arabia
- \* Correspondence: mahmoud.hafiez@physics.uu.se (M.A.-H.); ash02@fayoum.edu.eg (A.H.); Tel.: +46-72-831-37-11 (M.A.-H.)



**Citation:** Kamel, M.; Hanna, A.R.N.; Krellner, C.; Klingeler, R.; Abdellah, M.; Abdel-Hafiez, M.; Hassen, A.; Khalil, A.S.G.; Abdel-Baset, T.; Hassan, A. Synthesis, Optical, Magnetic and Thermodynamic Properties of Rocksalt  $\text{Li}_{1.3}\text{Nb}_{0.3}\text{Mn}_{0.4}\text{O}_2$  Cathode Material for Li-Ion Batteries. *Crystals* **2021**, *11*, 825. <https://doi.org/10.3390/cryst11070825>

Academic Editors: Anton Meden, Jiehua Liu, Fancheng Meng and Yi Sun

Received: 2 July 2021  
Accepted: 14 July 2021  
Published: 16 July 2021

**Publisher's Note:** MDPI stays neutral with regard to jurisdictional claims in published maps and institutional affiliations.



**Copyright:** © 2021 by the authors. Licensee MDPI, Basel, Switzerland. This article is an open access article distributed under the terms and conditions of the Creative Commons Attribution (CC BY) license (<https://creativecommons.org/licenses/by/4.0/>).

**Abstract:** Since the discovery of the reversible intercalation of lithium-ion materials associated with promising electrochemical properties, lithium-containing materials have attracted attention in the research and development of effective cathode materials for lithium-ion batteries. Despite various studies on synthesis, and electrochemical properties of lithium-based materials, fairly little fundamental optical and thermodynamic studies are available in the literature. Here, we report on the structure, optical, magnetic, and thermodynamic properties of Li-excess disordered rocksalt,  $\text{Li}_{1.3}\text{Nb}_{0.3}\text{Mn}_{0.4}\text{O}_2$  (LNMO) which was comprehensively studied using powder X-ray diffraction, transient absorption spectroscopy, magnetic susceptibility, and low-temperature heat capacity measurements. Charge carrier dynamics and electron–phonon coupling in LNMO were studied using ultra-fast laser spectroscopy. Magnetic susceptibility and specific heat data are consistent with the onset of long-range antiferromagnetic order at the Néel temperatures of 6.5 (1.5) K. The effective magnetic moment of LNMO is found to be  $3.60 \mu_B$ . The temperature dependence of the inverse magnetic susceptibility follows the Curie–Weiss law in the high-temperature region and shows negative values of the Weiss temperature 52 K (3), confirming the strong AFM interactions.

**Keywords:** Li-ion batteries;  $\text{Li}_{1.3}\text{Nb}_{0.3}\text{Mn}_{0.4}\text{O}_2$ ; magnetic susceptibility; specific heat

## 1. Introduction

Lithium-ion batteries (LIBs) are one of the most auspicious energy storage technologies for smartphones, laptops, electric hybrid vehicles, and renewable energy systems [1–3]. LIBs consist of two electrodes called the anode (negative) and the cathode (positive) separated by an electrolyte that can be a liquid or a solid [4,5]. Various alternative anode and

cathode materials have been developed for specific applications [6]. While in commercial LIBs, graphite is the most common example of anode material, various alternative intercalation-based materials as well as alloying-based ones such as tin (Sn), silicon (Si), germanium (Ge), and their alloys, and conversion reaction-based materials are investigated [7,8]. The first reported cathode materials are lithium manganese spinels, lithium metal oxides, and olivines [9]. Lithium-rich layered oxides were investigated with high voltage that can deliver an energy density of about (900 Wh/Kg) [10]. There is a tendency for Li-excess cathode materials design to a rocksalt structure to be characterized by complete or partial cation disorder [11]. The revelation of Li-ion cathode cation disordered rocksalt materials opens the way to consume a huge variety of  $3d$  and  $4d$  metals, in addition to metals used in layered Li-rich oxides. Compared to ordered cathode compounds, disordered cations give rise to specific characteristics, which are considered a challenge and opportunity at the same time to be applied in batteries. When the octahedral sites of a rocksalt structure are occupied with a random distribution of cations, octahedral deformation takes place due to their various valences and sizes. The created deformations must be accommodated in part by adjoining the octahedra that are edge allocation in rocksalt structure octahedra.

The positive electrodes synthesized using Earth-abundant Mn, Fe, and Ti ions have promising features regarding the cost and the natural plenty [12]. Various lithium metal oxides with the formula  $\text{LiMeO}_2$ , where  $Me$  is one or more metal species, present the cubic rocksalt (NaCl) crystal structure. As the sites of a face-centered cubic (FCC) lattice are filled by oxygen atoms, lithium, as well as other metal atoms (cations) fill the FCC sub-lattice of the octahedral interstices [13]. The disordered rocksalt structure (NaCl type or  $\alpha$ - $\text{LiFeO}_2$ ) can be obtained in the case that all cation sites are equivalent [13]. In addition, the magnetic and electronic properties of these compounds are governed by the kind of Li– $Me$  bond established, which consecutively relies upon the size as well as the electronic configuration of the  $Me^{3+}$  cation [14]. The Nb-based cathode material  $\text{Li}_{1.3}\text{Nb}_{0.3}\text{Mn}_{0.4}\text{O}_2$  (LNMO) was synthesized by N. Yabuuchi et al., hence, the substitution of  $\text{Mn}^{3+}$  in the formula  $\text{Li}_3\text{NbO}_4\text{-LiMe}^{3+}\text{O}_2$  has an effect on the clustering/ordering of niobium in the cubic close-packed (CCP) oxygen array where the ionic radii of  $\text{Mn}^{3+}$  in ranges between 0.76 Å for  $\text{Li}^+$  and 0.64 Å for  $\text{Nb}^{5+}$ . Consequently, this gives rise to the formation of cation-disordered rocksalt phases [15]. In a disordered rocksalt, both Li and transition metal (TM) occupy a (CCP) lattice of octahedral sites, and Li diffusion occurs by jumping between octahedral sites through an intermediate tetrahedral site [16–18]. The progress in the synthesis of electrochemically active lithium niobium manganese oxide stimulated us to study their magnetic properties and thermodynamics in detail. The resolving of the magnetic structure of this Li-ion battery cathode material will be advantageous to the quantitative predictions of electrochemical as well as electronic properties [19].

In order to meet a huge number of potential applications and any rational design of electrode materials, Li-ion materials need to be well-prepared in phase pure powder, and improvement of the current optical and thermodynamic data basis are also highly desirable. In this work, we report the synthesis and optical properties of LNMO, which were investigated using transient absorption spectroscopy (TAS) for the first time. Additionally, the magnetization behavior in a wide range of temperatures and magnetic fields, as well as the heat capacity at low temperatures, was discussed. The stability as well as the possibility of using LNMO in both low temperatures and high magnetic field atmospheres, which may affect the electrochemistry properties of this material, are also discussed.

## 2. Materials and Methods

### 2.1. Synthesis

In a particular LNMO cathode synthesis process, called molten-salt, a stoichiometric amount of  $\text{Li}_2\text{CO}_3$ ,  $\text{Mn}_2\text{O}_3$ ,  $\text{Nb}_2\text{O}_5$  (Sigma-Aldrich, Saint Louis, MO, USA, >99%) was milled together with ethanol as a solvent at 200 rpm for 12 h in a planetary ball mill (RETSCH PM100) using a zirconia jar with zirconia balls. An extra amount of  $\text{Li}_2\text{CO}_3$  of about 10–15 mol% was added to overcome the loss of Li during high-temperature sintering.

The powder was dried in the oven then mixed with KCl flux in a molar ratio of 2.5–5 between the flux and (TM) precursors. The resultant mixture was then heated at 950 °C for 12 h in an argon atmosphere [20]. A ramp rate of 4 °C/min was used for both heating and cooling steps. Figure 1a illustrates a schematic description of the heating and annealing process of the synthesis for LNMO. The annealing process of the sample has an important impact on the structure of the produced sample [21]. After the compilation of the process, KCl was dissolved in deionized water, and the final product was obtained via filtration and comprehensive washing with water, then it was dried in the vacuum oven [22].

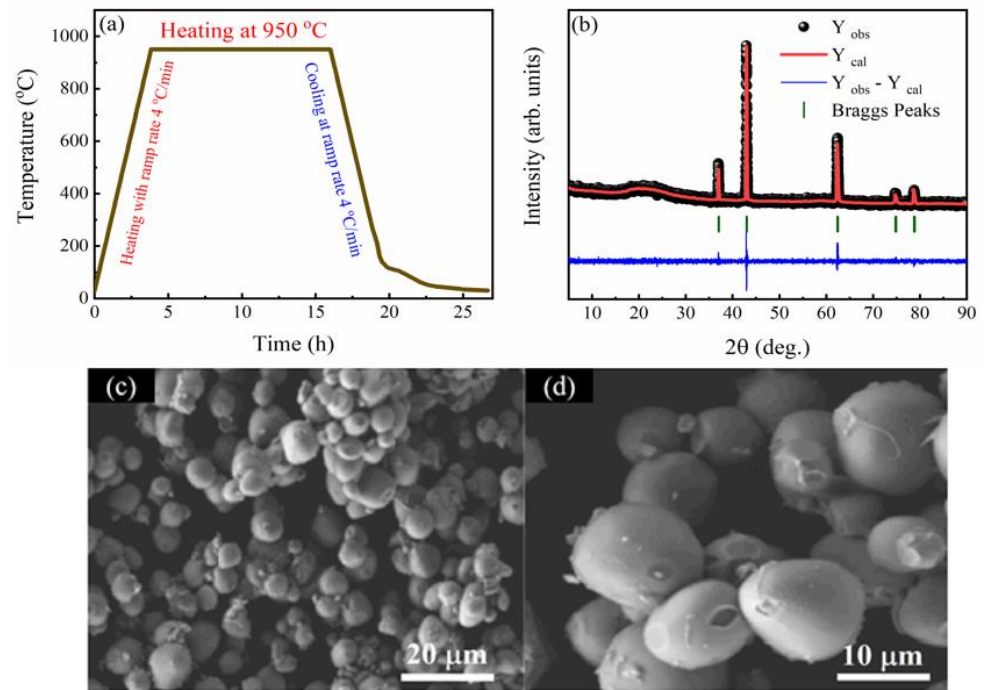


**Figure 1.** (a) A schematic description of the temperature profile for the synthesis of  $\text{Li}_{1.3}\text{Nb}_{0.3}\text{Mn}_{0.4}\text{O}_2$  in a tube furnace; (b) XRD Rietveld refinement profile. FE-SEM images of LNMO crystals; scale bar (c) 20  $\mu\text{m}$ ; (d) 10  $\mu\text{m}$ .

## 2.2. Characterization

The analysis of phase purity performed using laboratory X-ray diffraction (XRD) collected on Panalytical Empyrean X-ray diffractometer (Malvern Panalytical Ltd. Malvern, Worcestershire, UK) with ( $\text{Cu}, K_{\alpha 1}$ ) radiation (1.5406 Å), operated at an acceleration voltage of 40 kV and 40 mA current in the range of 4.99–89.90 Å. The XRD pattern was refined using FULLPROF software [23,24]. For the transient absorption spectroscopy, about 200 mg of the powder sample prepared as described above was sonicated in water for 25 min. Then, a suspension was diluted to obtain a transparent solution. The morphology of the LNMO polycrystalline sample was investigated by using the field-emission scanning electron microscopy (FE-SEM) (Zeiss FE-SEM Sigma 500 VP, Oberkochen, Germany). The transient absorption spectroscopy was carried out on laser-based spectroscopy. A coherent legend Ti: Sapphire amplifier (800 nm, 100 fs pulse length, 1 kHz repetition rate) was used. The used technique can be described as a UV light laser pulse of wavelength 345 nm with pulses width around 120 fs used to excite the sample (suspension in water), and at a certain time, another white light pulse (from 350 nm to 800 nm) was used to measure the change in the absorption of the sample. The output was split to give pump and probe beams. An optical parametric amplifier was used as a source for excitation pulses at a wavelength of 345 nm. The pulses in  $\text{CaF}_2$  crystal with wavelength 800 nm generate the probe pulses (a broad supercontinuum spectrum) and split to probe and reference pulses by a beam splitter. The probe and reference pulses were scattered in a spectrograph and a diode array

is used to detect these pulses. The instrumental response time is approximately 100 fs, the polarization of the pump was adjusted at a magic angle of  $54.7^\circ$  with respect to the probe beam [25–28]. Low temperature-specific heat and the magnetic properties of the investigated sample were measured by using the Quantum Design Physical Properties Measurement System (PPMS). The experiments were measured in a temperature range from 2.5 K to 300 K in the applied magnetic field up to 14 T. The AC susceptibility measurements were performed in a temperature range from 2 K to 20 K in applied AC magnetic fields and different frequencies.

### 3. Results and Discussion

The XRD shows that LNMO formed single phases in a disordered rocksalt structure. The Rietveld refinement was carried out using the disordered structural model with the cubic  $Fm\bar{3}m$  space group reported in the literature in the range of 4.99–89.90 Å. In the crystal structure, 4b sites are occupied by oxygen atoms forming a cubic close-packed structure, and Li, Nb, and Mn atoms are randomly distributed in 4a sites. The refinement profile of LNMO is shown in Figure 1b. A summary of crystal structural data is given in Table 1. The value of  $\chi^2$  is higher than unity, but it is also accepted as reported previously [29,30]. As illustrated in Figure 1c,d, the LNMO polycrystalline has a nearly spherical shape, indicating the good crystallization process. The average particle size distribution is calculated to be approximately 8.88  $\mu\text{m}$ .

**Table 1.** Crystallographic parameters were obtained from the refinement of XRD data for LNMO compound. Listed are Wyckoff positions, unit cell parameters, volume, Bragg factor  $R_{Bragg}$ , weighted profile  $R$ -factor  $R_{wp}$ , structure factor  $R_F$ , and goodness of fit  $\chi^2$ .

Space Group	$Fm\bar{3}m$	
Wyckoff position 4a (0, 0, 0)	Li occupancy	0.65 (1)
	Nb occupancy	0.15 (1)
	Mn occupancy	0.20 (1)
Wyckoff position 4b (0.5, 0.5, 0.5)	O occupancy	1.00
	$R_{Bragg}$ (%)	3.10
	$R_{wp}$ (%)	19.5
	$R_F$ (%)	1.93
	$\chi^2$	2.175

The excited state optical properties of the LNMO are achieved using fs laser based spectroscopy, where at a time ( $t$ ) equal to zero, electrons in the ground state ( $g$ ) are excited by the pump pulse with the energy of 5.06 eV creating a non-equilibrium population in the excited states. At a certain delay time after the excitation, the probe pulse detects the difference in the absorption of the excited state as shown in Figure 2a. Particularly in our sample, the pump pulse can promote electrons from the VBM (valance band maximum) to the CBM (conduction band minima). The depletion of the ground state by the pump pulse leads to the decrease in the transition from a ground state to excited states; this is the so-called ground state bleach (GSB) (Figure 2a, negative absorption) [31]. For a deep understanding of the bleach recovery dynamics, time traces at 378 nm were extracted. The bleach recovery dynamics of LNMO can be fitted using four distinct characteristic decay times, 19 ps, 23 ps, 290 ps, and a very slow component ( $>8.0$  ns) beyond our delay stage, through fitting with a triple exponential function, as shown in Figure 2b. Upon excitation of the LNMO with high energy photons, the electrons gain extra energy and become hot electrons [32]. As a result of the formation of these highly energetic hot electrons, they collide with each other as a way to dissipate their energy. These electrons refer to the ground state through carrier–carrier collisions; the additional energy is shared between the excited carriers [32]. The residual photon energy of the energy gap is dissipated as heat accompanied by lattice vibrations mediated by phonons [33]. The timescale of such a mechanism is in the

femtosecond scale specifically after the photoexcitation process [34]. In phonon-assisted processes, the rates of carrier capture depend on the lattice temperature [35–37]. Carrier generation/relaxation channel can be triggered by intense carrier–carrier interactions. In such a channel, the excess energy associated with an electron in the conduction band does not disperse through electron–phonon scattering [33]. Instead, this excess energy is delivered to the electron allocated in the valance band crossing the energy gap. This is called a collision-like process, in which intense carrier–carrier Coulomb coupling is the moderator of this process. The initial electron (exciton) produced by a high-energy photon is thought to exist in either a real or virtual short-lived state, from which it undergoes coherent or incoherent movement into a final multiexciton state [33]. The multiexcitons are generated by a single photon, decay on a picosecond timescale. This relatively fast decay is due to the Auger recombination process [33,38]. The electron-hole pairs recombination process is initiated within few picoseconds and stays for more than 100 ps. The hole contribution to the transient absorption (TA) signal is trivial because they have a high effective mass, the nanosecond decay of the TA kinetics for LNMO (beginning from 1000 ps) refers to the delay recombination process of the photoexcited electron-hole pairs [39]. After the excitation process, the ground state is bleached instantly; the transient spectra are recorded at different delay times, as shown in Figure 2a. There are positive absorption changes on the left side of the absorption band. A negative band referring to strong negative bleach appears around 380 nm [40].

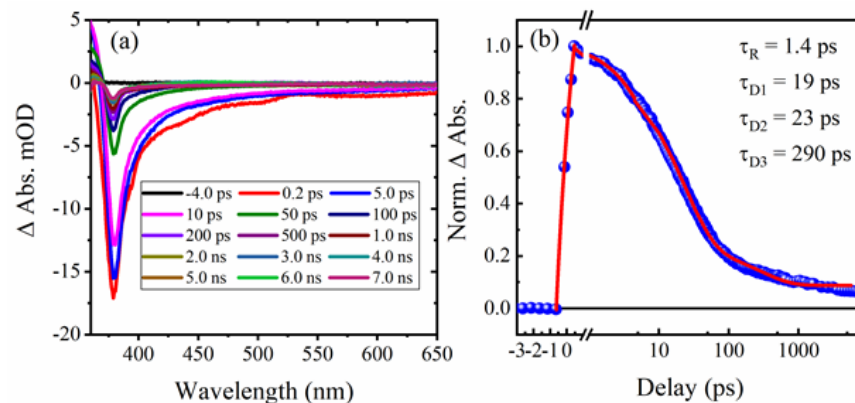


**Figure 2.** (a) Transient absorption spectra at different delay times; (b) transient absorption kinetics at the ground state bleach of  $\text{Li}_{1.3}\text{Nb}_{0.3}\text{Mn}_{0.4}\text{O}_2$ . Kinetic data are normalized to unity.

In order to further study the quality of the investigated system, as well as to obtain insights into its fundamental properties, magnetic properties up to 14 T were measured. In particular, the magnetic order is frequently a disturbance in battery materials associated with defects, structural disorder, and defeated magnetic interactions [41]. The molar susceptibility  $\chi_m$  versus the temperature (Figure S1a) shows an anomaly which is clear in the plot of the inverse of molar susceptibility ( $1/\chi_m$ ) versus the temperature (Figure S1b). Above the transition temperature of 6.5 K, Curie–Weiss behavior is verified as:

$$\chi = C_M / (T - \Theta) \quad (1)$$

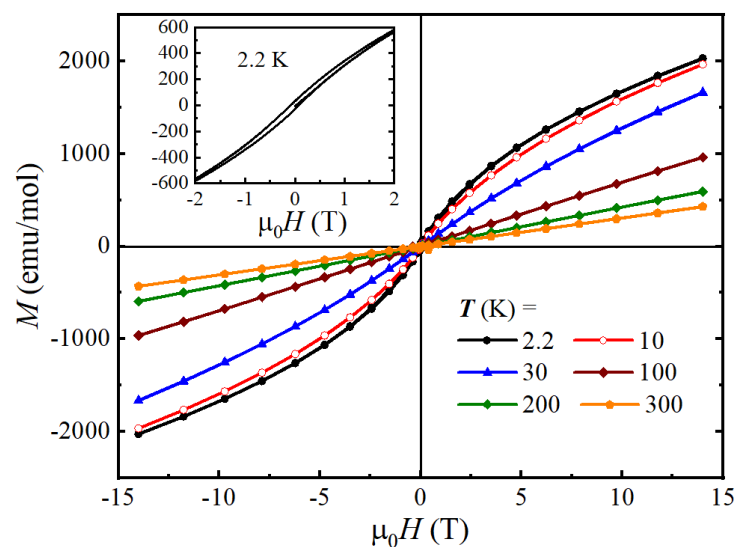
where  $C_M$ ,  $\Theta$  are the Curie constant and the Weiss temperature, respectively. As shown in Table 2, the Weiss temperature obtained from fitting in the temperature range 50–300 K shows a negative sign, reflecting dominant antiferromagnetic (AFM) interactions. This is due to the high numbers of cation-anion-cation (Mn–O–Mn) interactions that the octahedral-site cations are set on the opposite sides of a common anion, in case that they have a half-filled  $e_g$  orbital, they interact antiferromagnetically [42,43]. Upon applying a magnetic field up to 1T, the AFM ordering temperature  $T_N$  is suppressed and no anomaly indicating long-range order is observed down to 1.8 K.

**Table 2.** The fitted values of Weiss temperature, Curie constant, and effective magnetic moment for LNMO at  $\mu_0H = 0.1, 1,$  and  $9$  T from the fitting of  $1/\chi_m$  vs.  $T$  plots.

Parameter	$\mu_0H = 0.1$ T	$\mu_0H = 1$ T	$\mu_0H = 9$ T
$\Theta$ (K)	−52	−48	−56
$C_M$ (emu K/mol)	1.62	1.67	1.66
$\mu_{eff}(\mu_B)$	3.60 (0.4)	3.65 (0.5)	3.64 (0.5)

The Curie constant and the effective magnetic moment values at 0.1, 1, and 9 T are close to the calculated values for  $\text{Li}_{1.25}\text{Nb}_{0.25}\text{Mn}_{0.5}\text{O}_2$  by Jones et al. [21]. The reported values by Jones et al. are  $C_M = 1.8$  emu K/mol, and  $\mu_{eff}(\mu_B) = 3.8$  [21]. However, two factors might affect the effective magnetic moment value: (i) The disordered structure is somehow hindering the magnetic interaction between Mn ions [44]. (ii) A possible Jahn–Teller distortion of  $\text{Mn}^{3+}$  ions, where the configuration of  $\text{Mn}^{3+}$  ions is  $t_{2g}^3e_g^1$  [45,46]. Alonso et al. claimed that strong Jahn–Teller distortion is caused due to a single electron in  $e_g$  orbital of  $\text{Mn}^{3+}$  [47]. This distortion is required to decrease both repulsion energy between electrons and the degeneracy of the orbital [45,47].

The magnetization of LNMO as a function of the applied magnetic field at different temperatures up to a magnetic field of 14 T is shown in Figure 3 and is associated with a small hysteresis at low magnetic fields. Upon increasing the applied field, the magnetization keeps rising slowly with no saturation. The existence of hysteresis is strong at a low temperature of 2.2 K (the inset of Figure 3). The detected hysteresis in Fig. 3 at low magnetic fields and temperatures is indicative of the existence of a weak ferromagnetic (FM) phase. This FM phase can be created by the mixture valence of Mn-ions, for instance,  $\text{Mn}^{2+}$ ,  $\text{Mn}^{3+}$ , and  $\text{Mn}^{4+}$ . Consequently, the presence of these Mn-ions results in FM and AFM coupling in addition to some of canted AFM phases and impurity such as  $\text{LiMnO}_2$  [19].

**Figure 3.** The magnetization against the applied magnetic field up to 14 T at temperatures: 2.2; 10; 30; 100; 200; 300 K for  $\text{Li}_{1.3}\text{Nb}_{0.3}\text{Mn}_{0.4}\text{O}_2$ ; inset indicates the hysteresis loop at a temperature of 2.2 K.

To further understand the above-mentioned magnetic observations, AC susceptibility  $\chi_{AC}$  experiments were performed. The  $\chi_{AC}$  is composed of a real component  $\chi'$  that is related to the reversible magnetization process, remains in phase with the oscillating field, and an imaginary component  $\chi''$  that is associated with the losses due to the irreversible magnetization process as well as the absorbed energy from the field. The field dependence of the real part of  $\chi_{AC}$  as a function of the temperature is shown in Figure 4a. The measurements were taken at a frequency of 1 kHz and zero DC magnetic field; the phase transition confirms that at low temperatures the compound has AFM behavior. The temperature

was calculated from the differential ( $\partial(\chi'T)/\partial T$ ) as a function of the temperature curve;  $T_N = 5.3$  K, at zero AC magnetic field, is field dependent. With an increase in the applied magnetic field, there is a shift of the peak and  $T_N$  tends to decrease.

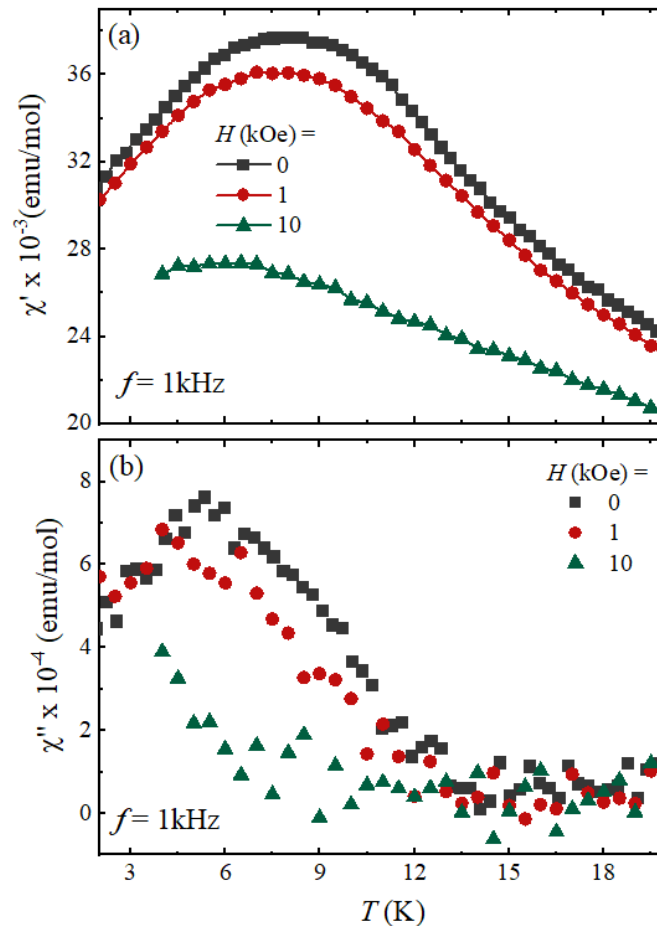


**Figure 4.** (a) The field dependence of the real part of AC susceptibility as a function of the temperature at different applied AC magnetic fields for LNMO, all data were taken at zero DC magnetic field; (b) the field dependence of the imaginary part of AC susceptibility as a function of the temperature at different applied AC magnetic fields for LNMO, all data were taken at zero DC magnetic field.

The frequency dependence of  $\chi'$  as a function of temperature is shown in Figure 5a, the measurements were taken at AC magnetic field amplitude of 1 kOe and zero DC magnetic field. The obtained Néel temperature is 5.0 K in the case of a frequency dependent measurement at a frequency of 3 kHz. From the upper panel of Figure 5, one can notice that the  $\chi'$  is frequency-independent.

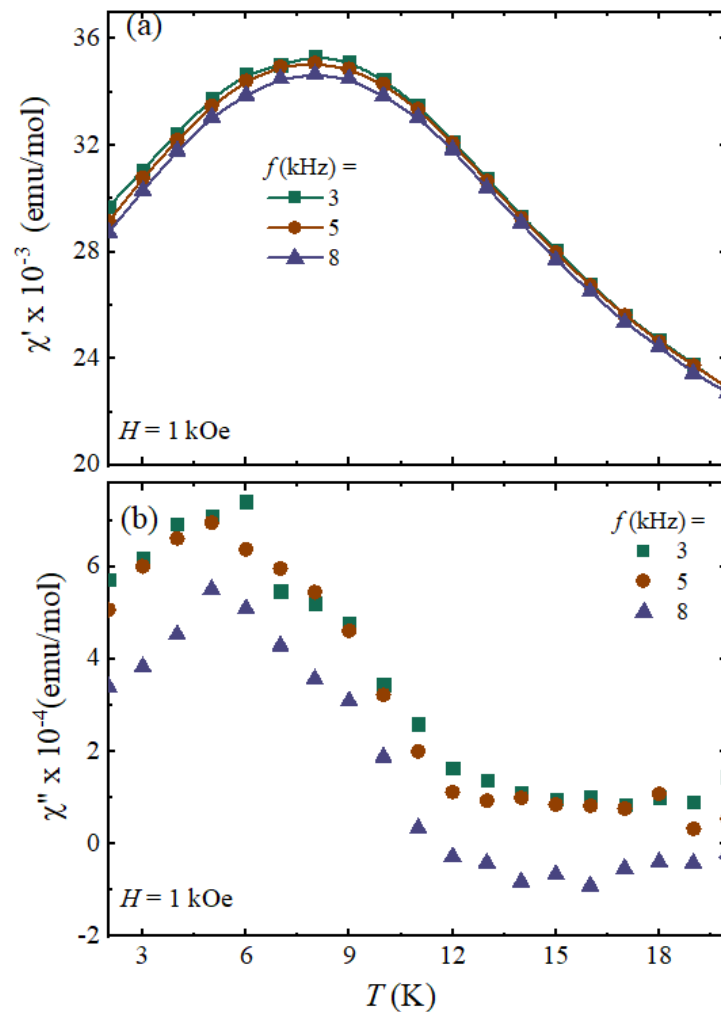


**Figure 5.** (a) The frequency dependence of the real part of AC susceptibility as a function of the temperature at different frequencies for LNMO, all data were taken at zero DC magnetic field; (b) the frequency dependence of the imaginary part of AC susceptibility as a function of the temperature at different applied frequencies for LNMO; all data were taken at zero DC magnetic field.

The field and frequency dependence of the real part of the AC susceptibility are consistent with the DC measurements and show that there is AFM order at low temperatures and paramagnetic behavior at higher temperatures. The imaginary part of the AC susceptibility,  $\chi''$  describes the losses associated with the irreversible magnetization process due to the existence of a small hysteresis loop; measuring this parameter at different AC magnetic fields and different frequencies indicates that  $\chi''$  is a field- and frequency-dependent, as illustrated in Figures 4b and 5b, respectively.

In order to further understand the low temperature behavior in our investigated system, we have performed heat capacity studies up to 9 T. The specific heat per temperature against the temperature at various magnetic fields is shown in Figure 6.



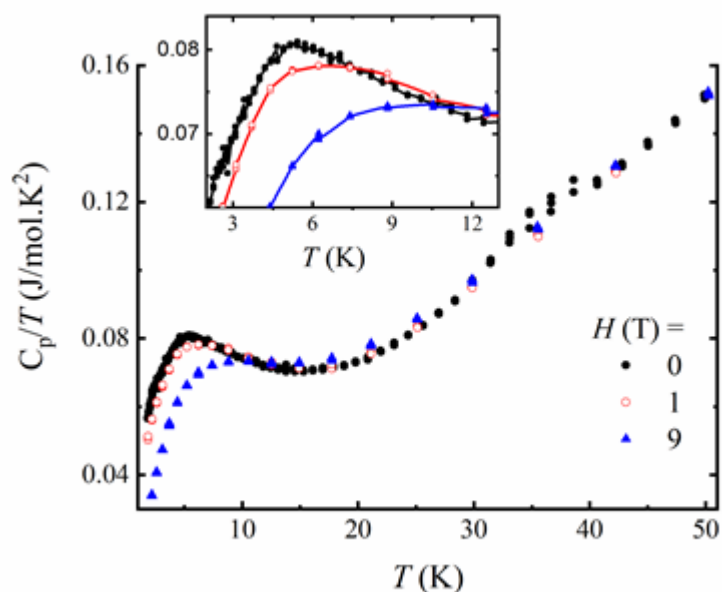


**Figure 6.** Temperature dependence of the specific heat at various applied fields at 0, 1, and 9 T for LNMO.

The classical Dulong–Petit limit is calculated to be  $C = 3nR \sim 99.76$  J/mol K (for  $n$  equals four atoms in the unit cell), where  $R$  is the gas constant equal to 8.314 J/mol.K. According to the Sommerfeld–Bethe theory of metals, the electronic specific heat is linear in temperature, while the lattice-specific heat is proportional to  $T^3$  in the low temperature limit [48,49]. The observed low value of the electronic specific heat-prefactor  $\gamma$  reflects the good quality of the synthesised materials, see Supplementary Materials Figure S2 [50–53]. At very low temperatures, specific heat data show a linear behavior indicating that there are no Schottky-like contributions in the sample above 1.8 K. The heat capacity data enable the calculation of the entropy  $S$  for LNMO. The entropy was derived by numerically integrating  $C_p/T$  between 0 and 50 K at magnetic fields of zero and 9 T.

#### 4. Conclusions

The optical, magnetic, and thermodynamic behavior of LNMO was investigated in detail. The ultra-fast dynamics of photoexcited carriers in LNMO shown for the fast multiexciton decay refers to the Auger recombination process. The sample has a significant negative bleach around a wavelength of 380 nm. From the magnetic measurements, an antiferromagnetic behavior is dominant at low temperatures with the coexistence of other phases such as weak ferromagnetic or canted antiferromagnetic phase, due to the interaction of Mn ions. The appearance of a hysteresis loop beside AC magnetic susceptibility measurements confirms these phenomena. The investigation of the Li-excess rocksalt cathode material LNMO behavior in extreme conditions is very important for their application. This is indispensable for enhancing the synthesis as well as the revealing of such a group of Li-ion battery cathode materials in the proceeding studies. The results of this study should significantly improve the data basis for thermodynamic calculations and simulations of processes utilizing lithium-ion battery materials.

**Supplementary Materials:** The following are available online at <https://www.mdpi.com/article/10.3390/cryst11070825/s1>, Figure S1: (a) The molar susceptibility and versus the temperature at the magnetic field of 0.1, 1T. (b) The inverse of molar susceptibility and versus the temperature of  $\text{Li}_{1.3}\text{Nb}_{0.3}\text{Mn}_{0.4}\text{O}_2$  at the magnetic field of 0.1T, the red line indicates the Curie–Weiss fitting; Figure S2: The specific heat per temperature as a function of the square of temperature at (a) 0 T, (b) 1 T, and (c) 9T, the inset indicates the fitting with Equation (2) at low temperatures.

**Author Contributions:** Conceptualization, M.K. and A.R.N.H.; methodology, C.K.; software, M.A.; validation, M.A.-H., R.K. and A.H. (Arafa Hassen); formal analysis, M.A.; investigation, M.A.-H.; resources, A.H. (Abdelwahab Hassan); data curation, M.A.-H.; writing—original draft preparation, M.K.; writing—review and editing, M.A.; visualization, T.A.-B.; supervision, A.H. (Abdelwahab Hassan); project administration, A.S.G.K.; funding acquisition, M.A.-H. All authors have read and agreed to the published version of the manuscript.

**Funding:** The authors acknowledge the financial support (Grant No. 23023) received from Science, Technology and Development Fund (STDF) Egypt (GERF funding program). M.A.-H and R.K. acknowledge the support by the Megagrant by the P220 program of the Government of Russia, project 075-15-2021-604. M.A.-H. acknowledges the financial support from the Swedish Research Council (VR) under project No. 2018-05393. The authors acknowledge the financial support by the Arab-German Young Academy of Sciences and Humanities (AGYA).

**Conflicts of Interest:** The authors declare no conflict of interest.

## References

1. Padhi, A.K.; NanjundaSwamy, K.S.; Goodenough, J.B. Phospho-olivines as Positive-Electrode Materials for Rechargeable Lithium Batteries. *J. Electrochem. Soc.* **1997**, *144*, 1188–1194. [[CrossRef](#)]
2. Deng, D.; Kim, M.-G.; Lee, J.Y.; Cho, J. Green energy storage materials: Nanostructured TiO<sub>2</sub> and Sn-based anodes for lithium-ion batteries. *Energy Environ. Sci.* **2009**, *2*, 818–837. [[CrossRef](#)]
3. Yun, Q.; Li, L.; Hu, Z.; Lu, Q.; Chen, B.; Zhang, H. Layered Transition Metal Dichalcogenide-Based Nanomaterials for Electrochemical Energy Storage. *Adv. Mater.* **2020**, *32*, e1903826. [[CrossRef](#)]
4. Goodenough, J.B.; Park, K.-S. The Li-Ion Rechargeable Battery: A Perspective. *J. Am. Chem. Soc.* **2013**, *135*, 1167–1176. [[CrossRef](#)]
5. Gangaja, B.; Nair, S.; Santhanagopalan, D. Surface-Engineered Li<sub>4</sub>Ti<sub>5</sub>O<sub>12</sub> Nanostructures for High-Power Li-Ion Batteries. *Nano-Micro Lett.* **2020**, *12*, 30. [[CrossRef](#)] [[PubMed](#)]
6. Doeff, M.M.; Chen, G.; Cabana, J.; Richardson, T.J.; Mehta, A.; Shirpour, M.; Duncan, H.; Kim, C.; Kam, K.C.; Conry, T. Characterization of Electrode Materials for Lithium Ion and Sodium Ion Batteries Using Synchrotron Radiation Techniques. *J. Vis. Exp.* **2013**, *10*, e50594. [[CrossRef](#)] [[PubMed](#)]
7. Ma, D.; Cao, Z.; Hu, A. Si-Based Anode Materials for Li-Ion Batteries: A Mini Review. *Nano-Micro Lett.* **2014**, *6*, 347–358. [[CrossRef](#)]
8. Chu, Y.; Xiong, S. Mixed transition-metal oxides@carbon core-shell nanostructures derived from heterometallic clusters for enhanced lithium storage. *Chin. Chem. Lett.* **2021**. [[CrossRef](#)]
9. Zhao, E.; Yu, X.; Wang, F.; Li, H. High-capacity lithium-rich cathode oxides with multivalent cationic and anionic redox reactions for lithium ion batteries. *Sci. China Ser. B Chem.* **2017**, *60*, 1483–1493. [[CrossRef](#)]
10. Hu, S.; Pillai, A.S.; Liang, G.; Pang, W.K.; Wang, H.; Li, Q.; Guo, Z. Li-Rich Layered Oxides and Their Practical Challenges: Recent Progress and Perspectives. *Electrochem. Energy Rev.* **2019**, *2*, 277–311. [[CrossRef](#)]
11. Wang, R.; Li, X.; Liu, L.; Lee, J.; Seo, D.-H.; Bo, S.-H.; Urban, A.; Ceder, G. A disordered rock-salt Li-excess cathode material with high capacity and substantial oxygen redox activity: Li<sub>1.25</sub>Nb<sub>0.25</sub>Mn<sub>0.5</sub>O<sub>2</sub>. *Electrochem. Commun.* **2015**, *60*, 70–73. [[CrossRef](#)]
12. Clément, R.J.; Lun, Z.; Ceder, G. Cation-disordered rocksalt transition metal oxides and oxyfluorides for high energy lithium-ion cathodes. *Energy Environ. Sci.* **2020**, *13*, 345–373. [[CrossRef](#)]
13. Urban, A.; Lee, J.; Ceder, G. The Configurational Space of Rocksalt-Type Oxides for High-Capacity Lithium Battery Electrodes. *Adv. Energy Mater.* **2014**, *4*, 4. [[CrossRef](#)]
14. Hewston, T.; Chamberland, B. A Survey of first-row ternary oxides LiMO<sub>2</sub> (M = Sc-Cu). *J. Phys. Chem. Solids* **1987**, *48*, 97–108. [[CrossRef](#)]
15. Yabuuchi, N.; Takeuchi, M.; Nakayama, M.; Shiiba, H.; Ogawa, M.; Nakayama, K.; Ohta, T.; Endo, D.; Ozaki, T.; Inamasu, T.; et al. High-capacity electrode materials for rechargeable lithium batteries: Li<sub>3</sub>NbO<sub>4</sub>-based system with cation-disordered rocksalt structure. *Proc. Natl. Acad. Sci. USA* **2015**, *112*, 7650–7655. [[CrossRef](#)] [[PubMed](#)]
16. Inoue, N.; Zou, Y. Electronic structure and lithium ion migration of La<sub>4/3-y</sub>Li<sub>3y</sub>Ti<sub>2</sub>O<sub>6</sub> using cluster model. *Solid State Ionics* **2005**, *176*, 2341–2344. [[CrossRef](#)]
17. Zakharova, G.; Volkov, V.; Täschner, C.; Hellmann, I.; Klingeler, R.; Leonhardt, A.; Büchner, B. Synthesis, characterization and magnetic properties of hexagonal (VO)<sub>0.09</sub>V<sub>0.18</sub>Mo<sub>0.82</sub>O<sub>3</sub>·0.54H<sub>2</sub>O microrods. *Mater. Lett.* **2011**, *65*, 579–582. [[CrossRef](#)]
18. Kang, K.; Ceder, G. Factors that affect Li mobility in layered lithium transition metal oxides. *Phys. Rev. B* **2006**, *74*, 74. [[CrossRef](#)]
19. Yang, F.; Xia, Z.; Huang, S.; Zhang, X.; Song, Y.; Xiao, G.; Shao, G.; Liu, Y.; Deng, H.; Jiang, D.; et al. High field phase transition of cathode material Li<sub>2</sub>MnSiO<sub>4</sub> for lithium-ion battery. *Mater. Res. Express* **2020**, *7*, 026104. [[CrossRef](#)]
20. Yabuuchi, N.; Nakayama, M.; Takeuchi, M.; Komaba, S.; Hashimoto, Y.; Mukai, T.; Shiiba, H.; Sato, K.; Kobayashi, Y.; Nakao, A.; et al. Origin of stabilization and destabilization in solid-state redox reaction of oxide ions for lithium-ion batteries. *Nat. Commun.* **2016**, *7*, 13814. [[CrossRef](#)]
21. Jones, M.A.; Reeves, P.J.; Seymour, I.D.; Cliffe, M.J.; Dutton, S.E.; Grey, C.P. Short-range ordering in a battery electrode, the ‘cation-disordered’ rocksalt Li<sub>1.25</sub>Nb<sub>0.25</sub>Mn<sub>0.5</sub>O<sub>2</sub>. *Chem. Commun.* **2019**, *55*, 9027–9030. [[CrossRef](#)] [[PubMed](#)]

22. Kan, W.H.; Chen, D.; Papp, J.K.; Shukla, A.K.; Huq, A.; Brown, C.M.; McCloskey, B.D.; Chen, G. Unravelling Solid-State Redox Chemistry in  $\text{Li}_{1.3}\text{Nb}_{0.3}\text{Mn}_{0.4}\text{O}_2$  Single-Crystal Cathode Material. *Chem. Mater.* **2018**, *30*, 1655–1666. [[CrossRef](#)]
23. Sosnowska, I.; Przeniosło, R.; Schäfer, W.; Kockelmann, W.; Hempelmann, R.; Wysocki, K. Possible deuterium positions in the high-temperature deuterated proton conductor  $\text{Ba}_3\text{Ca}_{1+y}\text{Nb}_{2-y}\text{O}_{9-\delta}$  studied by neutron and X-ray powder diffraction. *J. Alloys Compd.* **2001**, *328*, 226–230. [[CrossRef](#)]
24. Fernández, S.; Mesa, J.L.; Pizarro, J.L.; Lezama, L.; Arriortua, A.M.I.; Rojo, T. Two New Three-Dimensional Vanadium(III) and Iron(III) Phosphites Templated by Ethylenediamine:  $(\text{C}_2\text{H}_{10}\text{N}_2)_{0.5}[\text{M}(\text{HPO}_3)_2]$ . Ab Initio Structure Determination, Spectroscopic, and Magnetic Properties. *Chem. Mater.* **2002**, *14*, 2300–2307. [[CrossRef](#)]
25. Koyama, T.; Yoshimitsu, S.; Miyata, Y.; Shinohara, H.; Kishida, H.; Nakamura, A. Transient Absorption Kinetics Associated with Higher Exciton States in Semiconducting Single-Walled Carbon Nanotubes: Relaxation of Excitons and Phonons. *J. Phys. Chem. C* **2013**, *117*, 20289–20299. [[CrossRef](#)]
26. Abdellah, M.; Zhang, S.; Wang, M.; Hammarström, L. Competitive Hole Transfer from CdSe Quantum Dots to Thiol Ligands in CdSe-Cobaloxime Sensitized NiO Films Used as Photocathodes for  $\text{H}_2$  Evolution. *ACS Energy Lett.* **2017**, *2*, 2576–2580. [[CrossRef](#)]
27. Židek, K.; Zheng, K.; Ponseca, C.S.; Messing, M.E.; Wallenberg, L.R.; Chábera, P.; Abdellah, M.; Sundström, V.; Pullerits, T. Electron Transfer in Quantum-Dot-Sensitized ZnO Nanowires: Ultrafast Time-Resolved Absorption and Terahertz Study. *J. Am. Chem. Soc.* **2012**, *134*, 12110–12117. [[CrossRef](#)]
28. Zheng, K.; Židek, K.; Abdellah, M.; Zhang, W.; Chábera, P.; Lenngren, N.; Yartsev, A.; Pullerits, T. Ultrafast Charge Transfer from CdSe Quantum Dots to p-Type NiO: Hole Injection vs Hole Trapping. *J. Phys. Chem. C* **2014**, *118*, 18462–18471. [[CrossRef](#)]
29. Toby, B. R factors in Rietveld analysis: How good is good enough? *Powder Diffr.* **2006**, *21*, 67–70. [[CrossRef](#)]
30. Teo, P.T.; Anasyida, A.S.; Basu, P.; Sharif, N.M.J.M.S.F. Chemical, Thermal and Phase Analysis of Malaysia's Electric Arc Furnace (EAF) Slag Waste. *Mater. Sci. Forum* **2016**, *840*, 399–403. [[CrossRef](#)]
31. Flash photolysis and spectroscopy. A new method for the study of free radical reactions. *Proc. R. Soc. London. Ser. A Math. Phys. Sci.* **1950**, *200*, 284–300. [[CrossRef](#)]
32. Guo, B.; Sun, J.; Hua, Y.; Zhan, N.; Jia, J.; Chu, K. Femtosecond Laser Micro/Nano-manufacturing: Theories, Measurements, Methods, and Applications. *Nanomanuf. Metrol.* **2020**, *3*, 26–67. [[CrossRef](#)]
33. Klimov, V.I. Spectral and Dynamical Properties of Multiexcitons in Semiconductor Nanocrystals. *Annu. Rev. Phys. Chem.* **2007**, *58*, 635–673. [[CrossRef](#)] [[PubMed](#)]
34. Wang, H.; Zhang, C.; Rana, F. Ultrafast Dynamics of Defect-Assisted Electron–Hole Recombination in Monolayer  $\text{MoS}_2$ . *Nano Lett.* **2015**, *15*, 339–345. [[CrossRef](#)]
35. Chemla, D.S.; Miller, D.A.B. Room-temperature excitonic nonlinear-optical effects in semiconductor quantum-well structures. *J. Opt. Soc. Am. B* **1985**, *2*, 1155–1173. [[CrossRef](#)]
36. Henry, C.H.; Lang, D.V. Nonradiative capture and recombination by multiphonon emission in GaAs and GaP. *Phys. Rev. B* **1977**, *15*, 989–1016. [[CrossRef](#)]
37. Lax, M. Cascade Capture of Electrons in Solids. *Phys. Rev.* **1960**, *119*, 1502–1523. [[CrossRef](#)]
38. Židek, K.; Zheng, K.; Abdellah, M.; Lenngren, N.; Chábera, P.; Pullerits, T. Ultrafast Dynamics of Multiple Exciton Harvesting in the CdSe–ZnO System: Electron Injection versus Auger Recombination. *Nano Lett.* **2012**, *12*, 6393–6399. [[CrossRef](#)] [[PubMed](#)]
39. N., S.B.; Nĕmec, H.; Židek, K.; Abdellah, M.; Al-Marri, M.J.; Chabera, P.; Ponseca, C.; Zheng, K.; Pullerits, T. Time-resolved terahertz spectroscopy reveals the influence of charged sensitizing quantum dots on the electron dynamics in ZnO. *Phys. Chem. Chem. Phys.* **2017**, *19*, 6006–6012. [[CrossRef](#)]
40. Fălămaș, A.; Porav, S.A.; Tosa, V. Investigations of the Energy Transfer in the Phycobilisome Antenna of *Arthrospira platensis* Using Femtosecond Spectroscopy. *Appl. Sci.* **2020**, *10*, 4045. [[CrossRef](#)]
41. Chernova, N.A.; Nolis, G.M.; Omenya, F.O.; Zhou, H.; Li, Z.; Whittingham, M.S. What can we learn about battery materials from their magnetic properties? *J. Mater. Chem.* **2011**, *21*, 9865–9875. [[CrossRef](#)]
42. Kanamori, J. Theory of the Magnetic Properties of Ferrous and Cobaltous Oxides, I. *Prog. Theor. Phys.* **1957**, *17*, 177–196. [[CrossRef](#)]
43. Goodenough, J.B. An interpretation of the magnetic properties of the perovskite-type mixed crystals. *J. Phys. Chem. Solids* **1958**, *6*, 287–297. [[CrossRef](#)]
44. Rodriguez-Martinez, L.M.; Atfield, J.P. Cation disorder and size effects in magnetoresistive manganese oxide perovskites. *Phys. Rev. B* **1996**, *54*, R15622–R15625. [[CrossRef](#)] [[PubMed](#)]
45. Demirel, S.; Oz, E.; Altin, S.; Bayri, A.; Altin, E.; Avci, S. Enhancement of battery performance of  $\text{LiMn}_2\text{O}_4$ : Correlations between electrochemical and magnetic properties. *RSC Adv.* **2016**, *6*, 43823–43831. [[CrossRef](#)]
46. Fridrichová, J.; Bacik, P.; Ertl, A.; Wildner, M.; Dekan, J.; Miglierini, M. Jahn-Teller distortion of  $\text{Mn}^{3+}$ -occupied octahedra in red beryl from Utah indicated by optical spectroscopy. *J. Mol. Struct.* **2018**, *1152*, 79–86. [[CrossRef](#)]
47. Alonso, J.A.; Martínez-Lope, A.M.J.; Casais, M.T.; Fernández-Díaz, M.T. Evolution of the Jahn–Teller Distortion of  $\text{MnO}_6$  Octahedra in  $\text{RMnO}_3$  Perovskites (R = Pr, Nd, Dy, Tb, Ho, Er, Y): A Neutron Diffraction Study. *Inorg. Chem.* **2000**, *39*, 917–923. [[CrossRef](#)]
48. Majumdar, A.; VanGennep, D.; Brisbois, J.; Chareev, D.; Sadakov, A.V.; Usoltsev, A.S.; Mito, M.; Silhanek, A.V.; Sarkar, T.; Hassan, A.; et al. Interplay of charge density wave and multiband superconductivity in layered quasi-two-dimensional materials: The case of  $2\text{H-NbS}_2$  and  $2\text{H-NbSe}_2$ . *Phys. Rev. Mater.* **2020**, *4*, 084005. [[CrossRef](#)]

49. Beck, P.A.; Claus, H. Density of states information from low temperature specific heat measurements. *J. Res. Natl. Bur. Stand. Sect. A Phys. Chem.* **1970**, *74A*, 449–454. [[CrossRef](#)]
50. Subramani, T.; Navrotsky, A. Thermochemistry of cation disordered Li ion battery cathode materials, ( $M' = \text{Nb}$  and  $\text{Ta}$ ,  $M'' = \text{Mn}$  and  $\text{Fe}$ ). *RSC Adv.* **2020**, *10*, 6540–6546. [[CrossRef](#)]
51. Thomas, D.; Abdel-Hafiez, M.; Gruber, T.; Hüttl, R.; Seidel, J.; Wolter, A.U.; Buchner, B.; Kortus, J.; Mertens, F. The heat capacity and entropy of lithium silicides over the temperature range from (2 to 873) K. *J. Chem. Thermodyn.* **2013**, *64*, 205–225. [[CrossRef](#)]
52. Zybtshev, S.G.; Pokrovskii, V.Y.; Nasretdinova, V.; Zaitsev-Zotov, S.; Pavlovskiy, V.V.; Odobesco, A.B.; Pai, W.W.; Chu, M.-W.; Lin, Y.G.; Zupanič, E.; et al.  $\text{NbS}_3$ : A unique quasi-one-dimensional conductor with three charge density wave transitions. *Phys. Rev. B* **2017**, *95*, 035110. [[CrossRef](#)]
53. Tropper, P.; Troitzsch, U.; Dachs, E.; Benisek, A. Heat capacity measurements of  $\text{CaAlSiO}_4\text{F}$  from 5 to 850 K and its standard entropy. *Am. Miner.* **2018**, *103*, 1165–1168. [[CrossRef](#)]